

Article

MoO₃@MoS₂ Core-Shell Structured Hybrid Anode Materials for Lithium-Ion Batteries

Muhammad Faizan ¹, Sajjad Hussain ^{2,3} , Mobinul Islam ^{1,*}, Ji-Young Kim ⁴, Daseul Han ¹ , Jee-Hwan Bae ⁴ , Dhanasekaran Vikraman ⁵ , Basit Ali ¹ , Saleem Abbas ⁶ , Hyun-Seok Kim ⁵ , Aditya Narayan Singh ¹ , Jongwan Jung ^{2,3}  and Kyung-Wan Nam ^{1,*} 

¹ Department of Energy & Materials Engineering, Dongguk University, Seoul 04620, Korea; faizijaff@gmail.com (M.F.); endend42@naver.com (D.H.); basitalikhan077@gmail.com (B.A.); aditya@dongguk.edu (A.N.S.)

² Hybrid Materials Center (HMC), Sejong University, Seoul 05006, Korea; shussainawan@gmail.com (S.H.); jwjung@sejong.ac.kr (J.J.)

³ Department of Nanotechnology and Advanced Materials Engineering, Sejong University, Seoul 05006, Korea

⁴ Advanced Analysis & Data Center, Korea Institute of Science and Technology (KIST), Seoul 02792, Korea; jykim1128@kist.re.kr (J.-Y.K.); jhbae@kist.re.kr (J.-H.B.)

⁵ Division of Electronics and Electrical Engineering, Dongguk University-Seoul, Seoul 04620, Korea; v.j.dhanasekaran@gmail.com (D.V.); hyunseokk@dongguk.edu (H.-S.K.)

⁶ Centre for Energy Storage Research, Korea Institute of Science and Technology (KIST), Seoul 02792, Korea; saleem.abbas203@gmail.com

* Correspondence: mobin85@dongguk.edu (M.I.); knam@dongguk.edu (K.-W.N.)



Citation: Faizan, M.; Hussain, S.; Islam, M.; Kim, J.-Y.; Han, D.; Bae, J.-H.; Vikraman, D.; Ali, B.; Abbas, S.; Kim, H.-S.; et al. MoO₃@MoS₂ Core-Shell Structured Hybrid Anode Materials for Lithium-Ion Batteries. *Nanomaterials* **2022**, *12*, 2008. <https://doi.org/10.3390/nano12122008>

Academic Editors: Mojtaba Mirzaeian, Peter Hall, Desmond Gibson and Saule Aidarova

Received: 12 May 2022

Accepted: 7 June 2022

Published: 10 June 2022

Publisher's Note: MDPI stays neutral with regard to jurisdictional claims in published maps and institutional affiliations.



Copyright: © 2022 by the authors. Licensee MDPI, Basel, Switzerland. This article is an open access article distributed under the terms and conditions of the Creative Commons Attribution (CC BY) license (<https://creativecommons.org/licenses/by/4.0/>).

Abstract: We explore a phase engineering strategy to improve the electrochemical performance of transition metal sulfides (TMSs) in anode materials for lithium-ion batteries (LIBs). A one-pot hydrothermal approach has been employed to synthesize MoS₂ nanostructures. MoS₂ and MoO₃ phases can be readily controlled by straightforward calcination in the (200–300) °C temperature range. An optimized temperature of 250 °C yields a phase-engineered MoO₃@MoS₂ hybrid, while 200 and 300 °C produce single MoS₂ and MoO₃ phases. When tested in LIBs anode, the optimized MoO₃@MoS₂ hybrid outperforms the pristine MoS₂ and MoO₃ counterparts. With above 99% Coulombic efficiency (CE), the hybrid anode retains its capacity of 564 mAh g⁻¹ after 100 cycles, and maintains a capacity of 278 mAh g⁻¹ at 700 mA g⁻¹ current density. These favorable characteristics are attributed to the formation of MoO₃ passivation surface layer on MoS₂ and reactive interfaces between the two phases, which facilitate the Li-ion insertion/extraction, successively improving MoO₃@MoS₂ anode performance.

Keywords: core-shell structure; hybrid anode; MoS₂; MoO₃; hydrothermal synthesis

1. Introduction

For the ever-growing need for renewable resources, the energy storage area has attracted much attention to alleviate environmental catastrophe and energy difficulties caused by traditional fossil fuels [1]. In this regard, rechargeable Li-ion batteries (LIBs) have become by far the most promising energy storage systems for portable electronic devices and electric vehicles, due to their comparatively greater energy and power density, and long-cycle life [2–4]. Since the electrochemical properties of the active materials govern the LIB's performance, the development of new materials for LIBs is a crucial factor. Although LIBs are receiving growing attention, a graphite anode with a theoretical capacity of 372 mAh g⁻¹ cannot meet the challenging requirements for higher energy density [5].

To substitute for graphite, various anode materials have been explored to improve the electrochemical performance, including transition metal dichalcogenides (TMDs) [6–10], transition metal oxides (TMOs) [11–13], titanium-based materials [14,15], carbon nanomaterials [16,17], and their composite materials [18,19]. Alloying-type anodes (Si, Sn, Ge) are

the other alternative candidates that can replace graphite due to their very high theoretical capacity and relatively higher working potential, beneficial for reducing the risk of dendrite formation. However, the major drawback of these alloy-type anode materials is their massive volume expansion during cycling: for instance, Si expands up to 320%, leading to the failure of the active material. Extensive studies are ongoing to fix their volume expansion and stabilize them for LIBs [20–22]. Anode materials of the insertion type, such as carbonaceous materials and titanium-based oxides, have limited specific capacity. Compared to these insertion-type materials, conversion-type materials have a higher theoretical capacity of (600–1000 mAh g⁻¹) and may be ideal to meet the energy demand for large-scale energy storages [23]. Over the past several decades, TMOs, one of the conversion-type materials' families, have been studied extensively in LIBs [23,24]. Recent research has shifted focus from transition metal oxides (TMOs) to transition metal sulfides (TMSs), due to their better electrical conductivity, mechanical and thermal stability, and higher electrochemical activity [25,26]. The majority of TMSs have 2D layered structures with a chemical composition of MS_n (where $n = 1$ or 2 , and $M = \text{Mo}, \text{W}, \text{Ti}, \text{V},$ or Sn). With an analogous layered structure to that of graphite anodes, 2D TMSs enable high rate capability via facile Li insertion and extraction, while the strong covalent bonding within the layers provides structural rigidity and robustness, leading to stable cyclability [27]. Even the interlayer spacings of these layer-structured TMSs are wider than graphite (~3.3 Å), for example, ~6.2 Å for MoS₂, ~5.9 Å for SnS₂, and ~5.7 Å for VS₂ [28]. Using 2D TMSs with larger interlayer spacing can significantly reduce the diffusion barriers for Li-ions, and accommodate their expansion upon insertion. Most importantly, TMSs have a higher voltage platform compared to graphite anodes, which prevents the formation of lithium dendrites, and ensures their high safety [26]. Thanks to those advantageous properties, several TMS-based materials have shown larger Li storage capacities than graphite anodes, making them promising candidates for high-performance LIB anodes [25,26]. Molybdenum sulfide (MoS₂), one of the most intriguing TMSs, has been studied in a number of applications, including nanoelectronics, electrocatalysis, and energy storage systems [29,30]. The MoS₂ anode in LIBs undergoes an intercalation-assisted conversion reaction, where a Mo nanocrystal is embedded in the Li₂S matrix as the final lithiated product and displays a high theoretical capacity of 670 mAh g⁻¹ [28,31].

Although TMSs materials have many advantages, there are still challenges that need to be urgently solved. A particular problem is the sulfur dissolution in electrolytes caused by soluble polysulfide intermediates that occur during Li₂S formation/decomposition, which results in the loss of sulfur components, thus abruptly deteriorating the capacity [26]. Various composite strategies with transition metal oxides have been explored to address the above problems, such as the TiO₂@MoS₂ [32], SnO₂/SnS₂ [33], MoO₂/MoS₂ [34], MoO₃/MoS₂ [35], MoO₃/SnS₂ [36], Fe₂O₃/MoS₂ [37], and MoS₂/MnO [38], which showed improved electrochemical performance in LIBs. However, making composites with TMO materials would not be optimal for mitigating the severe shuttling of lithium polysulfide (LiPSs), since the sulfide electrode interface remains exposed to the electrolyte. Surface protection, such as introducing a metal oxide protective layer, might help reduce polysulfide shuttling by preventing the dissolution of intermediates and accumulation of the sulfur phase on the lithium counter electrode [39]. W.-H. Ryu et al. reported a WO₃ protective layer on WS₂ nanofiber anode material, which dramatically improves the cycling performance in a sodium-ion battery [40]. Therefore, the synergistic effect of structurally stable TMOs' surfaces with conductive TMS cores can be the key characteristic of potentially excellent electrochemical performance.

Herein, motivated by such synergetic effects of the TMO-covered TMS hybrid structure, we have proposed an in situ formation of MoO₃ on the MoS₂ TMS (denoted as MoO₃@MoS₂) by simple post-annealing of hydrothermally synthesized MoS₂. Structural characterizations have verified the formation of the MoO₃@MoS₂ hybrid structure. The MoO₃@MoS₂ hybrid anode has demonstrated much-improved cycling stability compared with the single-phase MoS₂ and MoO₃ counterparts, without sacrificing the high power and capacity.

2. Experimental Section

2.1. Synthesis of MoS₂, MoO₃@MoS₂, and MoO₃

The modified one-pot method was employed to synthesize the MoS₂ [41]. First, thiourea (SC(NH₂)₂, solution A), and ammonium molybdate ((NH₄)₂MoO₄, solution B) were dissolved in separate beakers for 30 min, followed by pouring solution B into solution A. This mixture was stirred moderately for another 30 min. Next, the transparent solution was placed into a 100 mL capacity Teflon-lined, stainless-steel autoclave, which was transferred to a convection oven programmed for the reaction at 200 °C for 12 h. After natural cooling to room temperature (RT), the black precipitates were collected, centrifuged with DI water and ethanol three times, then vacuum-dried at 100 °C for 1 h. Then, the as-synthesized MoS₂ was further calcined at (200, 250, and 300) °C at a 5 °C/min rate in a box furnace. As per the structural results, the (200, 250, and 300) °C annealed samples were denoted as MoS₂, MoO₃@MoS₂, and MoO₃, respectively.

2.2. Material Characterizations

High-resolution powder X-ray diffraction (HRPD) data were collected at the 9B beamline of the Pohang Acceleration Laboratory (PAL, Pohang, South Korea), using a monochromated X-ray with a wavelength (λ) of 1.5183 Å. The Raman spectra were collected using a Renishaw inVia system with an excitation wavelength of 532 nm. X-ray photoelectron spectroscopy (XPS) measurements (Ulvac PHI X-tool spectrometer) were performed with Al-K α X-ray radiation, to investigate the chemical and valence states of the materials. The Mo K-edge X-ray absorption spectroscopy (XAS) spectra were measured at the Pohang Accelerator Laboratory (PAL) 8C beamline, in transmission mode, and processed with Athena software. The morphology and microstructure of the powders were analyzed by field-emission scanning electron microscopy (FE-SEM, Regulus 8230, HITACHI) and transmission electron microscopy (TEM, Talos F200X, ThermoFisher). Thermogravimetric analysis (TGA) of the as-prepared sample was carried out on a NETZSCH (STA 449F3, Selb, Germany) thermal analyzer with a heating rate of 10 °C/min in open-air conditions. Electrical conductivity was evaluated using a Loresta-GP low-resistivity meter (MCP-T610, Mitsubishi Chemical corp.). The sample porosity characteristics were determined by nitrogen adsorption and desorption measurements at 77 k (Micromeritics, Norcross, GA, USA).

2.3. Electrochemical Measurements

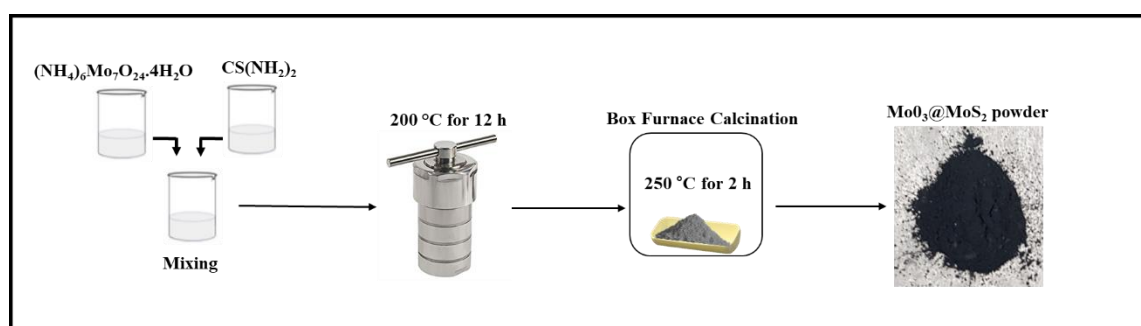
The 2032-coin cells with a two-electrode configuration were used to perform the electrochemical experiments. The MoS₂, MoO₃@MoS₂, and MoO₃ powder samples were thoroughly mixed with conductive carbon black and poly(vinylidene) fluoride (PVDF) binder dissolved in N-methyl pyrrolidone (NMP) solution in an 8:1:1 weight ratio to make a viscous slurry. The working electrode was prepared using a doctor blade casting on a Cu foil current collector. The electrode loading level was controlled to be ~ 2.27 mg cm⁻² of active material. We used a TMAX roll press machine for calendaring. The density of electrodes was calculated to be 1.8997 g/cm³. The coin cells were assembled inside a glove box filled with Ar gas, with a Li metal counter electrode, a separator (Celgard 3501), and 1.0 M LiPF₆ in a 1:1 (v:v) ratio of ethylene carbonate/dimethyl carbonate with 3% FEC additive as the electrolyte. After stabilizing the coin cell for 24 h, electrochemical tests were performed using a Neware (CT-4008-5 V 10 mA-164) battery cycler at RT. A Bio-Logic electrochemical system (VMP-3) was used to measure the cyclic voltammetry (CV). The cells were cycled at different current densities (35 to 700) mA g⁻¹ between the potential window of (0.01–3.00) V. A cyclic voltammetry (CV) test was done under a 0.1 mV s⁻¹ scan rate within the potential window of (0.01–3.00) V. A PGSTAT 302 electrochemical workstation (Metrohm Autolab) was employed to measure the electrochemical impedance spectroscopy (EIS) in the frequency range (100 kHz to 0.01 Hz) at an open-circuit voltage (OCV).

3. Results and Discussion

Scheme 1 shows a schematic of the hydrothermal reaction followed by post-annealing in the air to synthesize MoO₃@MoS₂ hybrid material. The SEM images in Figure 1a,b demonstrate that the as-prepared MoS₂ exhibits a 2D-sheet-like morphology, reflecting its 2D hexagonal structure, similar to the previous reports [27,41]. These nanosheets are twisted together due to their curved morphology, which causes many voids between them. When annealed at 250 °C in the air, the surface of the 2D-sheet-like structures appears somewhat disrupted, associated with the potential formation of a MoO₃ layer (Figure 1c,d). The presence of Mo, S, and O in the EDS (Energy dispersive spectroscopy) pattern (Figure S1 of the Supplementary Information (SI)) indicates that the MoO₃@MoS₂ hybrid has been successfully formed. Evidently, the MoO₃@MoS₂ hybrids exhibit a morphology that shows a mixture of sheet-like and particle-like characteristics, such that the surfaces appear excessively rough, in apparent contrast to the smooth surface of the pristine MoS₂ nanosheets (Figure 1a). On the other hand, when the sample is further annealed at 300 °C, different sizes of cuboid-shaped grains are observed for pure MoO₃ formation (Figure 1e,f).

Synchrotron-based high-resolution powder diffraction (HRPD) was used to investigate the crystal structure of the MoS₂, MoO₃@MoS₂, and MoO₃ samples, as presented in Figures 2a and S2. The characteristic peaks of the MoS₂ sample annealed at 200 °C match very well with those of the hexagonal-structured 2D MoS₂ with the space group *P6₃/mmc* (JCPDS # 37–1492), while the intense XRD peaks for MoO₃ annealed at 300 °C confirm the formation of a highly crystalline α -MoO₃ phase with an orthorhombic structure and space group *Pbnm* (JCPDS # 35–0609). Notably, the MoO₃@MoS₂ sample annealed at 250 °C exhibits the diffraction peaks corresponding to both hexagonal MoS₂ and orthorhombic MoO₃ phases, verifying the hybrid structure formation. Notably, the MoO₃ peak intensity in the MoO₃@MoS₂ hybrid was relatively lower than that of the MoO₃ sample heated at 300 °C, suggesting the relatively lower content of the MoO₃ than the MoS₂. Figure S3a–c depicts the HRPD profile matching data of MoS₂, MoO₃@MoS₂, and MoO₃. The as-prepared hybrid material perfectly matches and contains the well-positioned diffraction peaks of MoS₂ and MoO₃. The lattice volume (*v*) of the MoS₂ component in MoO₃@MoS₂ hybrid decreased by 0.71% when it was annealed at 250 °C, as shown in Table S1. The lattice volume contraction is due to the formation of the MoO₃ layer, which compresses the core lattice [42]. In the hybrid, however, the MoS₂ phase is not sufficiently crystallized to allow Rietveld refinement for calculating the weight fraction of MoS₂ and MoO₃.

Furthermore, the Raman spectra in Figure 2b also prove the successful formation of the MoO₃@MoS₂ hybrid, agreeing with the XRD results. The MoS₂ spectrum presents the E_{2g}¹ (380.5 cm⁻¹) and A_{1g} (406 cm⁻¹) peaks corresponding to the in-plane and out-of-plane vibration modes of Mo-S, respectively [43]. The characteristic peak for the MoO₃ phase positioned at 664 cm⁻¹ belongs to B_{2g}/B_{3g} mode associated with the triply coordinated oxygen stretching in the 3MoO₆⁶⁻ [44]. The Raman spectrum of the MoO₃@MoS₂ demonstrates the signature of both MoS₂ and MoO₃ peaks, confirming the formation of the MoO₃@MoS₂ hybrid.



Scheme 1. Schematic of MoO₃@MoS₂ synthesis.

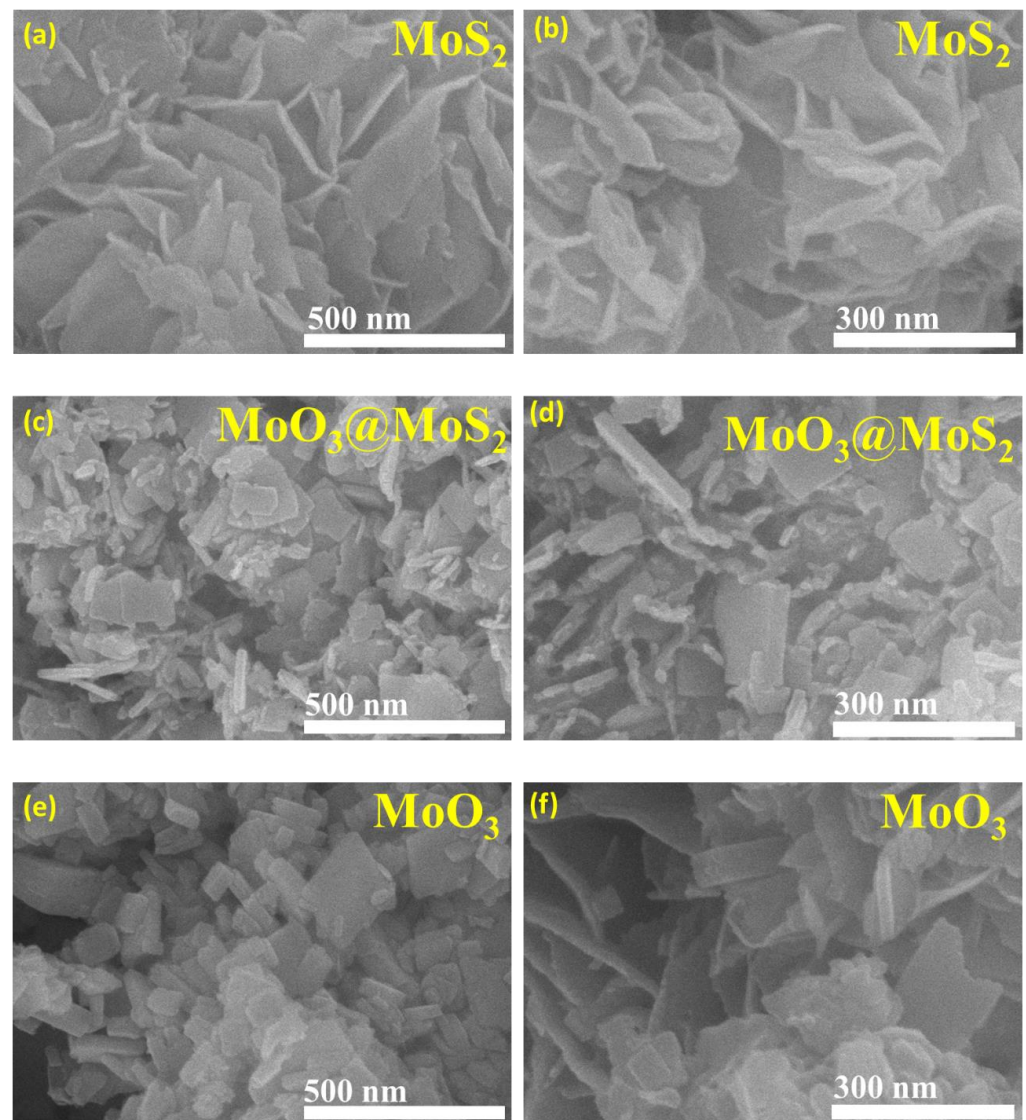


Figure 1. FE-SEM images for (a,b) MoS₂, (c,d) MoO₃@MoS₂, and (e,f) MoO₃.

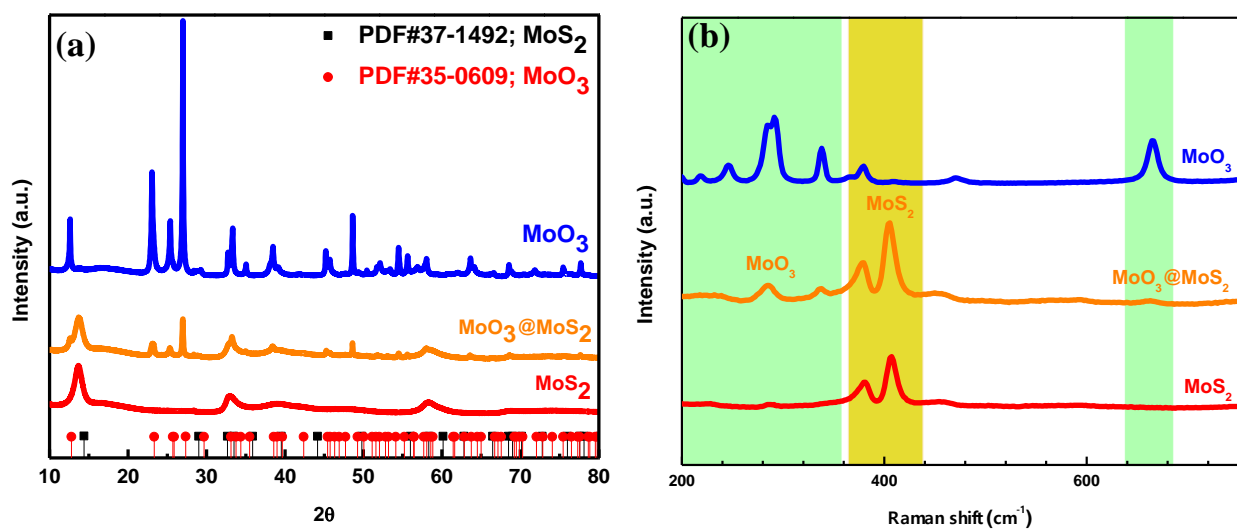


Figure 2. (a) HRPD and (b) Raman spectra of MoS₂, MoO₃@MoS₂, and MoO₃.

XPS analysis was further performed to verify the chemical and electronic state at the sample's surface. Figure S4 of the SI shows the survey spectrum of the MoO₃@MoS₂ sample, supporting the concurrent presence of Mo, S, and O elements in the prepared sample. Figure 3a compares the high-resolution Mo 3d core level XPS spectrum for the MoS₂, MoO₃@MoS₂, and MoO₃ samples. Two distinct peaks displayed at 229.3 and 232.5 eV for MoS₂ correspond to Mo⁴⁺ 3d_{3/2} and 3d_{5/2} states, respectively. The high-resolution XPS spectrum of the MoO₃ profile exhibits the 236.1 and 233.5 eV peaks corresponding to the Mo⁶⁺ 3d_{3/2} and 3d_{5/2} states, respectively [45]. The Mo 3d region of the MoO₃@MoS₂-XPS profile reveals the presence of mixed Mo⁶⁺ and Mo⁴⁺ oxidation states. Interestingly, the intensity of two distinct peaks at 236.1 and 233.5 eV associated with the MoO₃ is predominant in the XPS spectra of the MoO₃@MoS₂ sample. Meanwhile, the two other peaks correspond to Mo⁴⁺ oxidation states associated with the MoS₂ shift to low binding energy, suggesting that electron transfer occurs between MoO₃ and MoS₂ [37]. This finding implies that the hybrid sample shows a strong coupling between the MoS₂ and MoO₃ interface. Figure 3b shows the S 2p XPS region of MoS₂, MoO₃@MoS₂, and MoO₃. For MoS₂, the deconvoluted S 2p profile exhibits the doublet at 162.1 and 163.2 eV, while MoO₃ shows no peak, confirming that only O and Mo are present in the MoO₃ sample. The MoO₃@MoS₂ hybrid displays a noticeable shift of the two S 2p peaks to a lower binding energy, revealing that the MoO₃ surface layer influences the valence states of the S species. The spectrum also includes a weak and broad peak at 168.9 eV, likely corresponding to the S-O bond formed during the post-annealing in air [46,47]. In Figure 3c, the deconvoluted O 1s region clearly establishes the Mo-O bonding in the MoO₃ and MoO₃@MoS₂ hybrid samples [48–50]. Environmental sources and complete oxidation at 300 °C are attributed to the observed weak and strong O 1s peaks of MoS₂ and MoO₃, respectively. When compared to the MoO₃@MoS₂ hybrid sample, the shallow O 1s peak supports the evolution of the MoO₃ oxide layer at the MoS₂ surface.

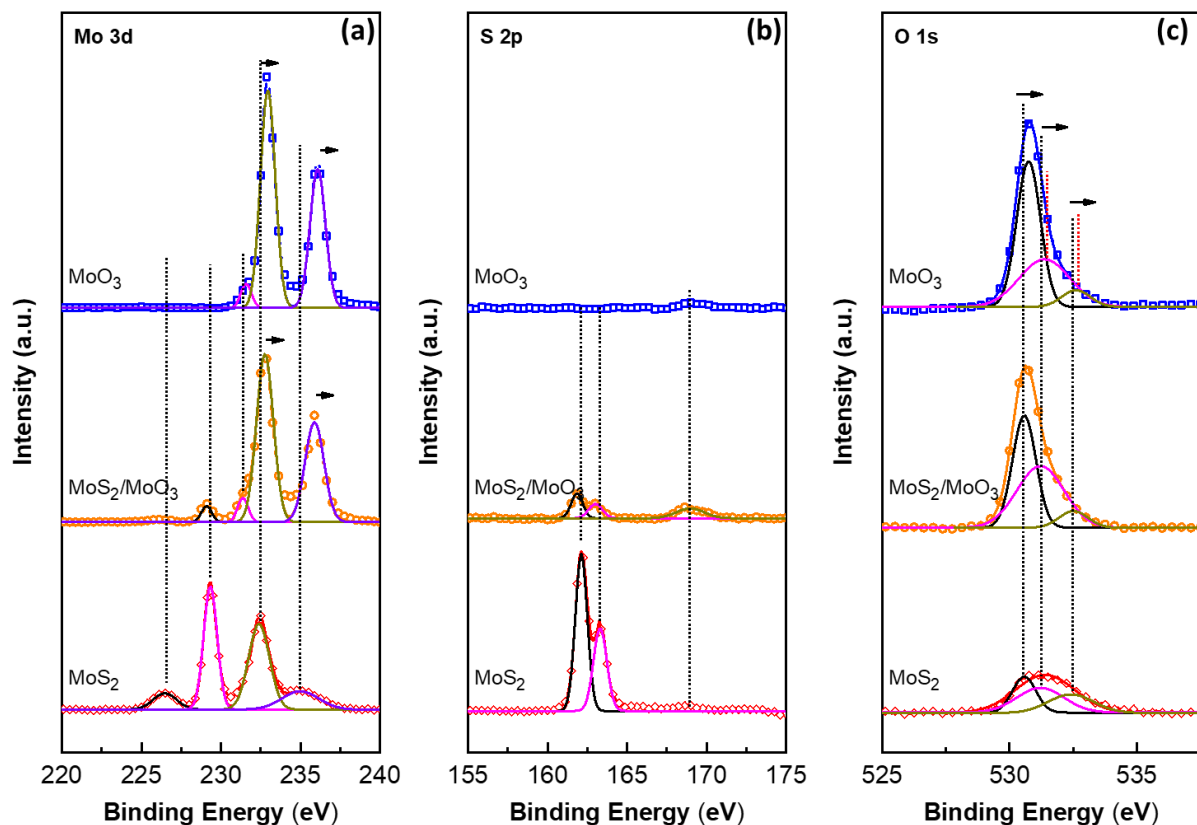


Figure 3. (a) Mo 3d, (b) S 2p, and (c) O 1s XPS spectra of MoS₂, MoO₃@MoS₂, and MoO₃.

Overall, the Raman results are in complete accordance with the XRD results, but XPS results show somehow opposite behavior regarding the crystal structure of the MoO₃@MoS₂ hybrid sample. While XRD is a bulk probe (detected in the micrometer range), XPS is a surface probe (of a few nanometers). Based on the XPS data recorded in the Mo 3d and S 2p regions, the peak density associated with the sulfur phase dropped while the peak density for the oxide phase strengthened (Figure 3a,b), suggesting the MoS₂ surface almost converted to MoO₃. XRD results show that the MoS₂ phase predominates over the MoO₃ phase in bulk, while the XPS peaks show that the oxide phase prevails on the surface of the MoO₃@MoS₂ hybrid. The ratio of the integral area between oxygen and sulfur obtained from XPS survey data is 9:1 (O2p/S2p~90.42/9.58). This ratio asserts our statement that the surface of MoS₂ almost converted to MoO₃. In contrast, we observed 1.5 wt% loss after the oxidation process above 250 °C in the TGA curve of as-synthesized MoS₂ (Figure S5). Based on the calculation (see the SI), the bulk MoO₃:MoS₂ ratio is approximately 1.5:8.5 in the MoO₃@MoS₂ hybrid. This finding confirms the results of XRD and Raman. Furthermore, another bulk probe technique, X-ray absorption spectroscopy (XAS), also exhibits a similar tendency to XRD. The Mo K-edge position of the MoO₃@MoS₂ hybrid is much closer to that of MoS₂ spectra, as shown in Figure 4a. There are two notable peaks in the Fourier-transformed extended X-ray absorption fine structure (FT-EXAFS) spectra (without phase correction) of MoS₂ at approximately 1.91 and 2.92 Å, corresponding to Mo-S and Mo-Mo interaction in the first and second coordination shells, respectively [51]. As expected, the FT-EXAFS spectrum of MoO₃@MoS₂ matches very well with MoS₂, rather than MoO₃. This finding further confirms that the MoS₂ phase dominates the core of the MoO₃@MoS₂ hybrid, validating our XRD and Raman results. In light of these results, we conclude that the precise control of the post-annealing procedure (i.e., 250 °C in air) produces a MoO₃ surface layer on the MoS₂ backbone. Scheme 2 graphically presents the structural changes during the post-annealing. The optimization of the post-calcination temperature (~250 °C) is critical in tuning the surface oxidation degree of the MoO₃@MoS₂ hybrid, as the sulfide phase completely transforms into MoO₃ at 300 °C.

The morphology and phase information of MoS₂, MoO₃@MoS₂, and MoO₃ nanostructures are further elucidated by TEM/EDS analysis, as depicted in Figure 5. The typical sheet-like morphology of MoS₂ is further confirmed by TEM images (Figure 5a,b). The selected area electron diffraction (SAED) patterns in Figure 5c displays three diffraction rings for the (002), (100), and (103) lattice planes, indicating the hexagonal MoS₂ polycrystalline structure (JCPDS # 37-1492). After introducing MoO₃, the sheet-like structures of MoS₂ are partially broken, as seen in Figure 5d,e. An enlarged TEM image shows d₀₀₂ edges of the MoS₂ phase (Figure S6 of the SI). The MoO₃@MoS₂ diffraction ring intensity appears weaker and blurrier than MoS₂ on the SAED (Figure 5f), but likely relates to the MoS₂ phase. This indicates that the sulfide phases are oxidized on the surface and turn into MoO₃ phases, which disrupts the MoS₂ crystallinity. These observations are consistent with the XRD and XPS results (Figures 2a and 3). In comparison, the cuboid-shaped MoO₃ (Figure 5g,h) shows entirely different SAED patterns (Figure 5i). The TEM-EDS elemental mapping (Figure 5j) indicates the uniform distribution of the Mo, S, and O species in the MoO₃@MoS₂ particles. It is evident that sulfur (red) exists within the particle's core bodies, while oxide (green) is present at the surface, entirely covering the core. Figure S7a-c shows the BET sorption isotherm of MoS₂, MoO₃@MoS₂, and MoO₃ samples. The type-III isotherm profiles and absence of a hysteresis loop suggest the low porosity of all the materials. The BET surface area of MoS₂, MoO₃@MoS₂, and MoO₃ is only 8.71, 8.42, and 9.85 m² g⁻¹, respectively (Table S2). The pore distribution curve (Figure S7d) indicates the presence of only interparticle porosity.

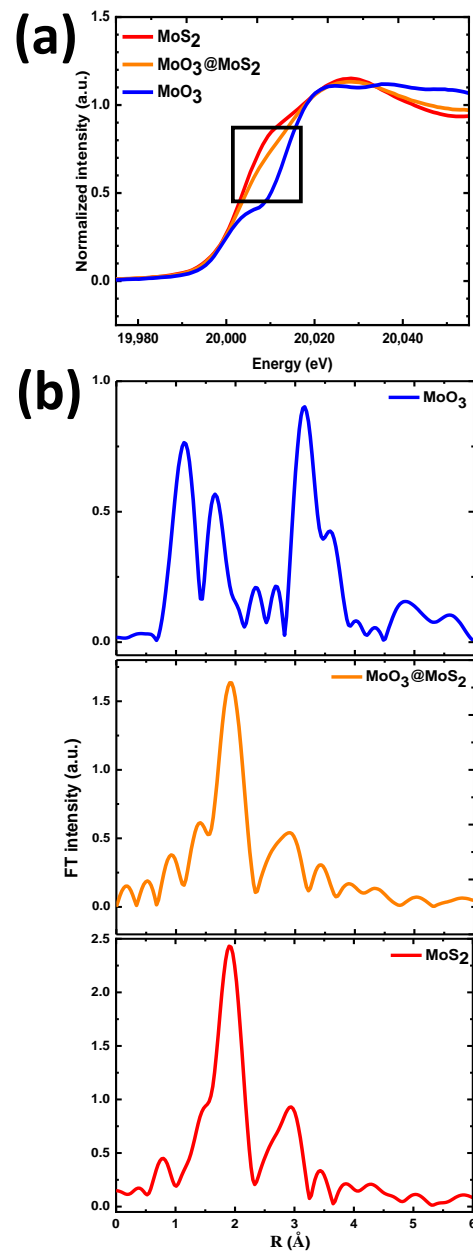
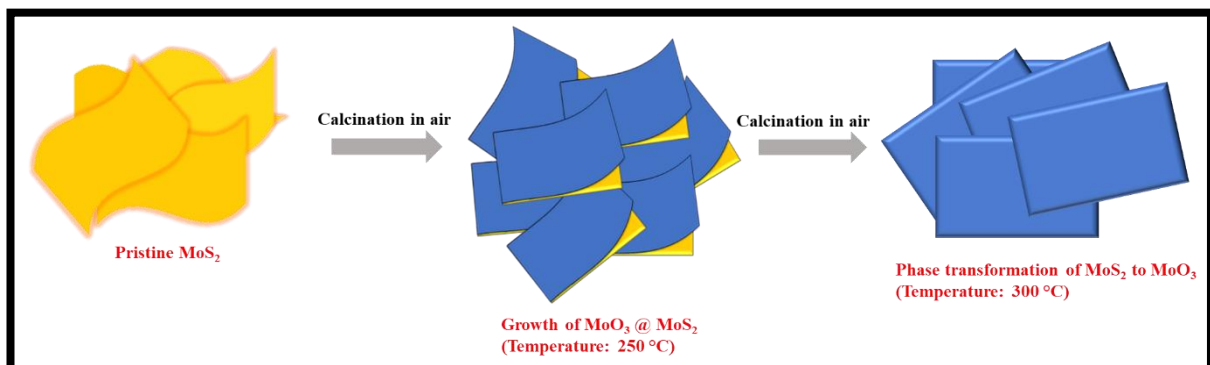


Figure 4. Mo K-edge (a) XANES, and (b) FT-EXAFS spectra, of MoS₂, MoO₃@MoS₂, and MoO₃.



Scheme 2. Schematic of the phase transformation of MoS₂ between (~200 and ~300) °C.

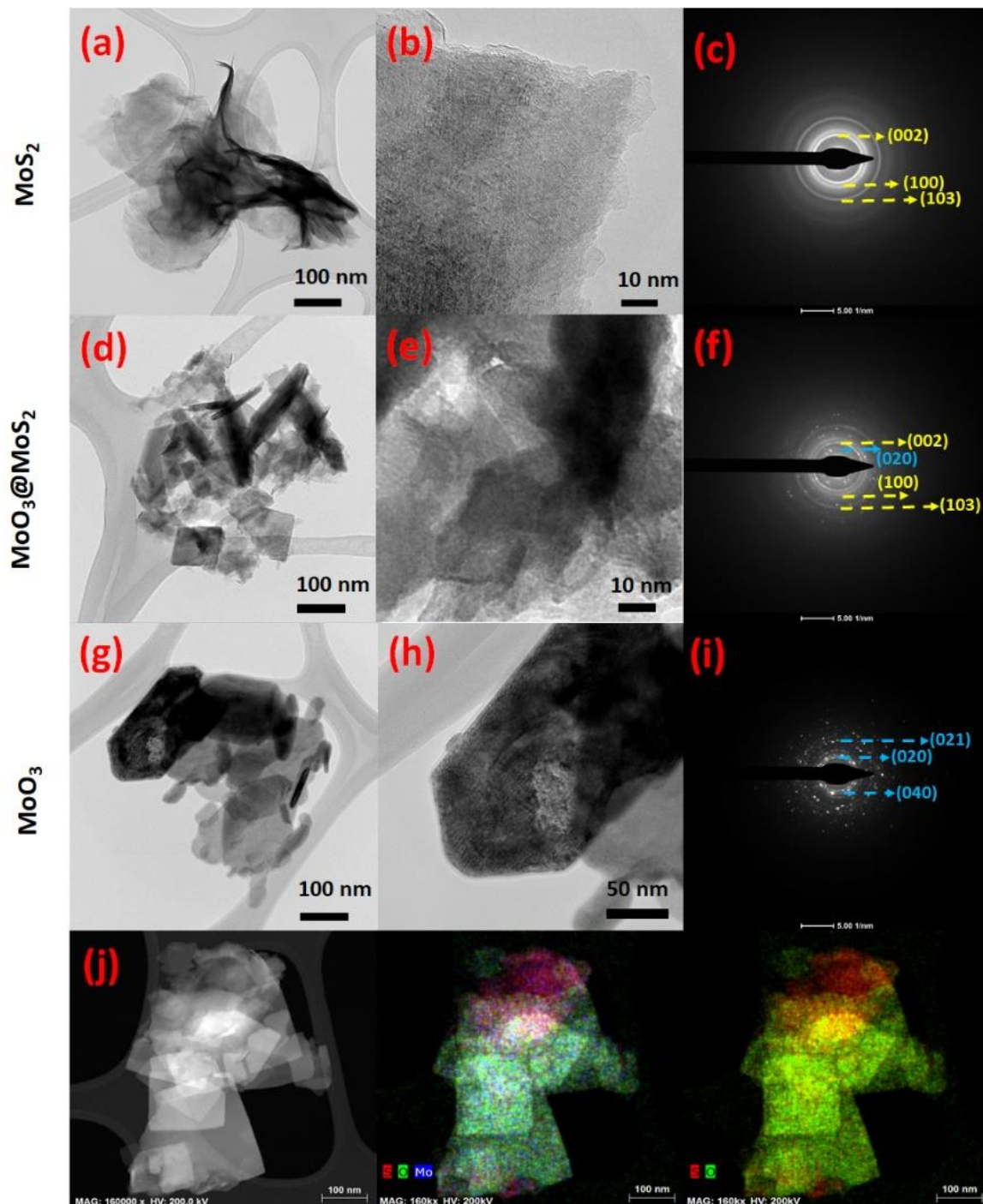


Figure 5. TEM images and corresponding SAED pattern of (a–c) MoS_2 , (d–f) $\text{MoO}_3@MoS_2$, (g–i) MoO_3 . (j) TEM-EDS mapping image of $\text{MoO}_3@MoS_2$.

The electrochemical performance of each sample was tested in the LIB half-cells. The cyclic voltammetry (CV) of the $\text{MoO}_3@MoS_2$ hybrid was measured in the voltage window of 0.01 to 3.0 V with a sweep speed of 0.1 mV s^{-1} ; the result is shown in Figure 6a. A reduction peak is located at 1.01 V, attributed to the Li-ion insertion between MoS_2 layers and forming Li_xMoS_2 . Another peak positioned at 0.46 V is linked to the conversion reaction of Li_xMoS_2 to $(\text{Mo} + \text{Li}_2\text{S})$ [52]. These two reduction peaks shifted to a higher potential at about 1.91 and 1.15 V from the second cycle onwards. A shallow reduction peak at 0.1 V in the first cycle is the characteristic of solid electrolyte interface (SEI) formation. In the

anodic scan, peaks located at 1.73 and 2.29 V are linked to the reverse conversion reaction of $\text{Mo} + \text{Li}_2\text{S}$ into MoS_2 , respectively [34]. The position of the oxidation peaks remains unchanged in the following cycles. Notably, a small irreversible peak at 2.11 V is found in the first cathodic scan, indicating Li^+ intercalation into MoO_3 crystals to generate Li_xMoO_3 [53]. Following the first cycle, the corresponding reduction peak did not occur, suggesting that the MoS_2 is the predominant participant in the redox activity of the $\text{MoS}_2@/\text{MoO}_3$ hybrid anode. Therefore, it seems that the main function of MoO_3 is to stabilize MoS_2 . Further, the observed CV shows excellent reversibility from the 2nd to 5th cycles, which indicates superior cycling stability. The observed area under the curve of the $\text{MoO}_3@/\text{MoS}_2$ composite is higher than that of its pristine components (shown in Figure S8a,b in SI), indicating enhanced capacity. Figure 6b shows the galvanostatic discharge/charge (GCD) curve of $\text{MoO}_3@/\text{MoS}_2$ at the current density of 50 mA g^{-1} ; where the initial cycle reveals a remarkably high reversible (charge) capacity of $\sim 721 \text{ mAh g}^{-1}$. The observed capacity is close to the theoretical limit of $\text{MoO}_3@/\text{MoS}_2$ ($\sim 737 \text{ mAh g}^{-1}$). Based on the TGA data (Figure S5), we estimated the theoretical capacity as described in SI. Figure S9a–c shows the extended discharge/charge curves for MoS_2 , $\text{MoO}_3@/\text{MoS}_2$, and MoO_3 . When comparing the GCD curves of the three samples, it can be seen that the $\text{MoO}_3@/\text{MoS}_2$ hybrid outperforms the MoS_2 and MoO_3 counterparts in terms of cycling stability during 100 cycles, establishing its good stability as an active anode material for LIBs. Moreover, the similar trend of the charge/discharge curve for the hybrid anode from the second cycle indicates excellent electrochemical stability and conversion reversibility. In contrast, the charge/discharge capacities for the pristine MoS_2 gradually deteriorated over the 100 cycles. Figure 6c further illustrates the difference in cyclability among MoS_2 , $\text{MoO}_3@/\text{MoS}_2$, and MoO_3 anodes. The $\text{MoO}_3@/\text{MoS}_2$ anode possesses a higher initial charge (reversible) capacity than MoS_2 and MoO_3 , with a Coulombic efficiency (CE) of 80.5, 83.5, and 41.5%, respectively. There is a significant decrease in capacity for the first few cycles of the $\text{MoO}_3@/\text{MoS}_2$ anode. This phenomenon is commonly observed in the conversion-based anode materials, because during the discharge-charge process of the initial cycles, the SEI layer is not fully formed. This accounts for the low CE and capacity loss during initial cycles, as reported in previous studies [6–20]. The CV result described earlier also accords with this behavior. However, after a few cycles, the $\text{MoO}_3@/\text{MoS}_2$ anode started to stabilize and the Coulombic efficiency improved, which is a marked difference from the pristine MoS_2 or MoO_3 anodes. The obtained result highlights the superior Li^+ storage performance of the $\text{MoO}_3@/\text{MoS}_2$ anode. In addition, the $\text{MoO}_3@/\text{MoS}_2$ anode demonstrates a notably higher capacity ($\sim 564 \text{ mAh g}^{-1}$) than that of MoS_2 ($\sim 34 \text{ mAh g}^{-1}$) and MoO_3 ($\sim 434 \text{ mAh g}^{-1}$) at the end of 100 cycles. Compared with an anode made of pure MoS_2 , the $\text{MoO}_3@/\text{MoS}_2$ anode exhibits enhanced electrochemical properties because of the MoO_3 passivation layer on the surface of the conductive MoS_2 . When we disassembled cells for MoS_2 and $\text{MoO}_3@/\text{MoS}_2$ electrodes after 30 cycles, we observed the active material residue on the lithium foil (counter electrode) for the MoS_2 anode sample. Contrary to this, there was no active material found on lithium foil (counter electrode) in the hybrid anode sample (Figure S10). During the charge/discharge cycles, MoS_2 and $\text{MoO}_3@/\text{MoS}_2$ anodes undergo a steady conversion process, as evidenced by their Mo K-edge EXAFS spectra measured after the 50 cycles. The FT-EXAFS spectra peaks from their 50th cycle remain almost identical to those from their pristine state (Figure S11). Figure 6d and S12 show the rate capability of the $\text{MoO}_3@/\text{MoS}_2$ hybrid and its pristine components (MoS_2 and MoO_3). As the current densities increase from 35 to 700 mA g^{-1} , the capacities of the $\text{MoO}_3@/\text{MoS}_2$ anode decrease; but when the current density is returned to its initial value (35 mA g^{-1}), the active material retains a high-capacity value ($\sim 434 \text{ mAh g}^{-1}$). The pure MoO_3 shows very poor rate performance compared to MoS_2 , which is attributed to the poor conductive characteristics of the oxide material, as presented in Table 1.

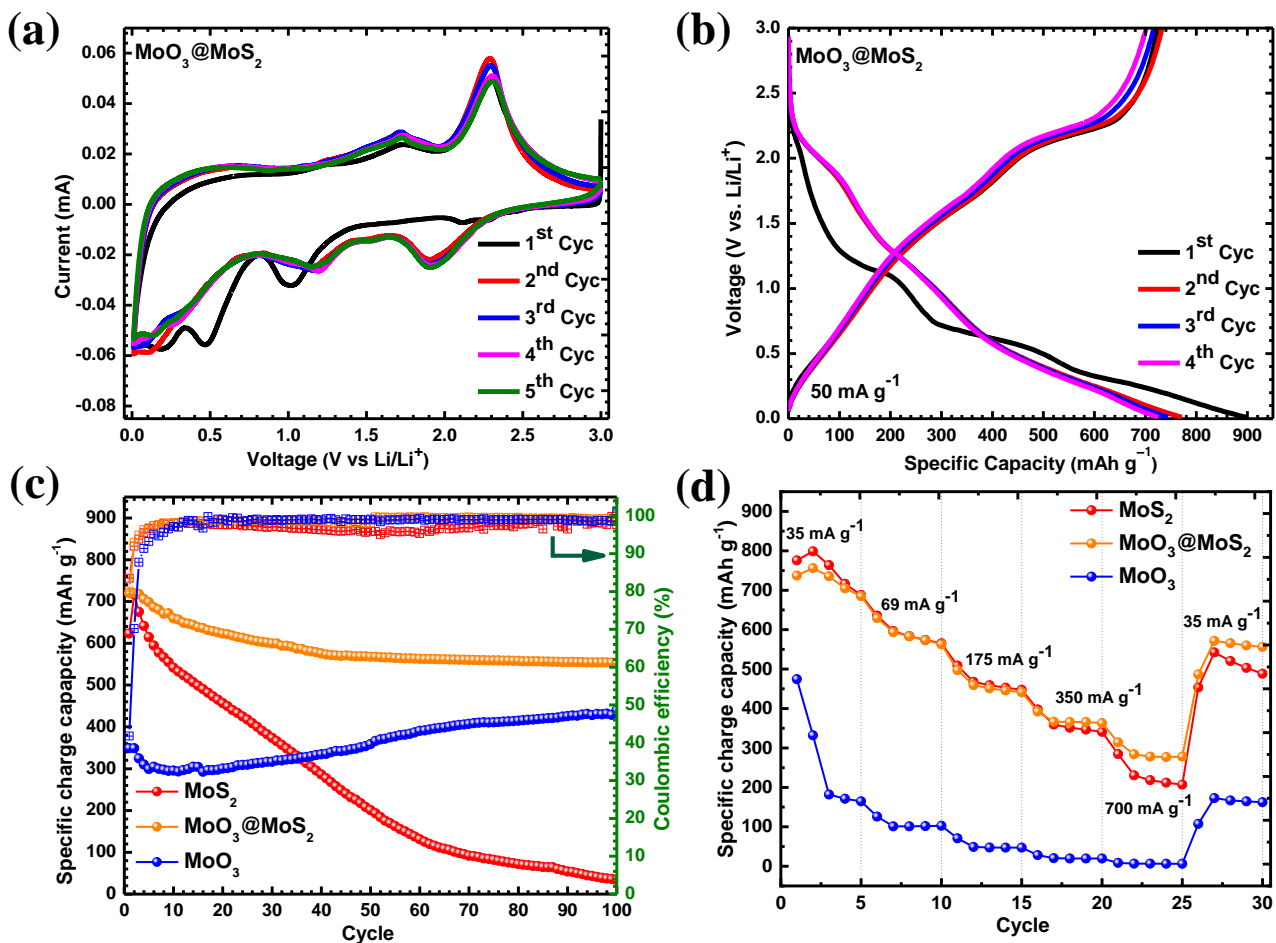


Figure 6. (a) CV and (b) discharge/charge profiles of MoO₃@MoS₂ between (0.01 and 3.00) V. (c) Comparative cycling performance at a current density of 50 mA g⁻¹ and (d) rate performance of MoS₂, MoO₃@MoS₂, and MoO₃ anodes in LIBs.

Table 1. Electrical conductivity measurement (by four-point probe) results.

Serial No.	Material	Average Electrical Conductivity ($\mu\text{S}\cdot\text{cm}^{-2}$)
01	MoS ₂	5.2442
02	MoO ₃ @MoS ₂	0.6443
03	MoO ₃	0.0282

Figure 7a,b shows the electrochemical impedance spectroscopy (EIS) data with a fitted profile, measured after the 1st and 30th cycles, respectively. An equivalent electrical circuit is presented, where R_s is the solution resistance, R_{ct} is the charge transfer resistance, W is Warburg impedance, while the (CPE1 and CPE2) are the constant phase elements. Figure 7a clearly shows that the semi-circle of the MoO₃@MoS₂ hybrid anode Nyquist plot is much smaller than its counterparts (MoS₂ and MoO₃) after the 1st cycle. The calculated solution resistance (R_s) and charge transfer resistance (R_{ct}) of the hybrid anode are 2.392 and 284.308 Ω , respectively, which are lower than those of MoS₂ and MoO₃ (Table S3). Furthermore, after 30 cycles, the resistance of all the materials increases, but among them, MoO₃@MoS₂ shows much smaller resistivity. The hybrid anode material shows a lower R_{ct} value (304.539 Ω) among the three materials (Table S4) thanks to the chemically resistive nature of oxide, which protects the sulfide phase from the dissolution into the electrolyte.

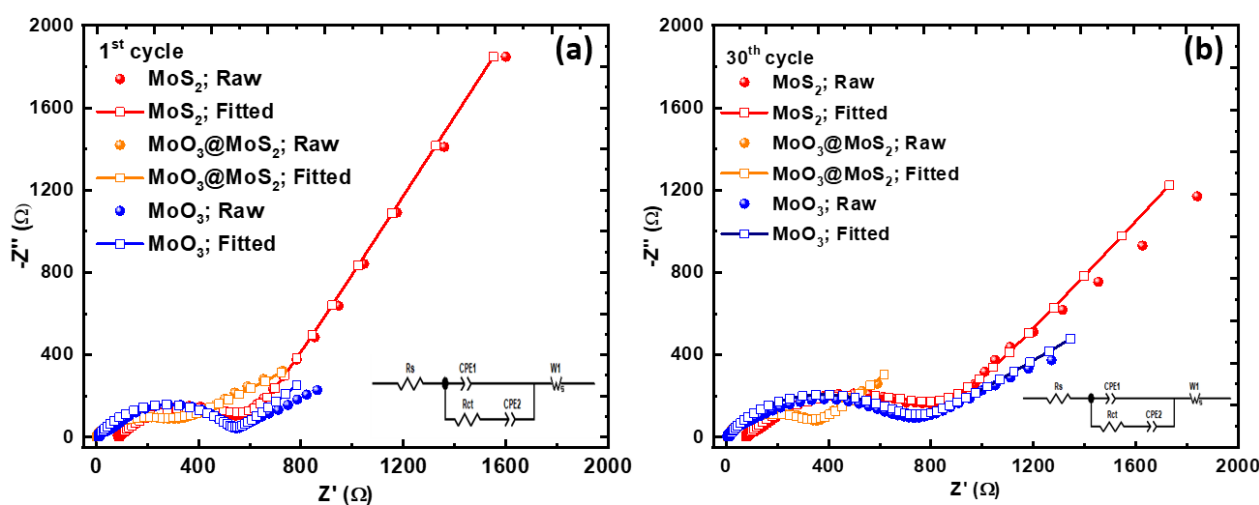


Figure 7. EIS profiles of MoS₂, MoO₃@MoS₂, and MoO₃ (a) after the 1st cycle, and (b) after the 30th cycle.

4. Conclusions

A novel, in situ approach to the synthesis of a hybrid nanostructure has been successfully optimized. This involves a two-step process of a hydrothermal reaction with subsequent air annealing. The successful formation of the MoS₂ core-MoO₃ shell hybrid structure was verified by XRD, Raman, XPS, and XAS results. SEM and TEM studies reveal the morphology evolution with the growth of an oxide layer on the bulk sulfide, which facilitates stable cycling stability without sacrificing the high capacity and fast-charging performance. The MoO₃@MoS₂ hybrid anode delivered an excellent specific charge capacity of 721 mAh g⁻¹, a good rate-capability of 278 mAh g⁻¹ at 700 mA g⁻¹, and the retained capacity was ~564 mAh g⁻¹ after 100 cycles, with excellent (~99%) Coulombic efficiency. The outstanding performance of the hybrid anode results from the synergistic interaction between the passivating layer of MoO₃, which eradicates the excessive dissolution of active material, and the conducting core of MoS₂, which ensures smooth electronic conduction. The work presented in this paper provides a simple, two-step, facile method to synthesize different transition metal oxide/sulfide hybrid nanostructures.

Supplementary Materials: The following supporting information can be downloaded at: <https://www.mdpi.com/article/10.3390/nano12122008/s1>, Figure S1: EDX spectrum of MoO₃@MoS₂; Figure S2: XRD of (a) MoS₂ and (b) MoO₃, including MoO₃@MoS₂, compared with their corresponding standard (PDF) data; Figure S3: Profile matching of HRPD data of (a) MoS₂, (b) MoO₃@MoS₂, and (c) MoO₃; Figure S4: XPS survey spectrum of MoS₂, MoO₃, and MoO₃@MoS₂; Figure S5: Thermogravimetric analysis (TGA) curve of as-synthesized MoS₂ in air; Figure S6: HR-TEM image of the MoO₃@MoS₂ sample; Figure S7: (a–c) BET and (d) corresponding BJH profile of MoS₂, MoO₃, and MoO₃@MoS₂; Figure S8: CV curves of (a) MoS₂ and (b) MoO₃ anodes; Figure S9: GCD curves of the (a) MoS₂, (b) MoO₃@MoS₂ and (c) MoO₃; Figure S10: Photos of Li counter electrodes for the MoS₂ and MoO₃@MoS₂ electrodes half-cells; Figure S11: Ex-situ Mo K-edge FT-EXAFS spectra of MoS₂ and MoO₃@MoS₂ after 50 cycles; Figure S12: The galvanostatic voltage profiles (rate performance) of MoS₂ and MoO₃@MoS₂ anodes at different current densities in LIBs; Table S1: Unit cell parameters of MoS₂, MoO₃@MoS₂, and MoO₃; Table S2: Result of BET analysis of MoS₂, MoO₃@MoS₂, and MoO₃; Table S3: Fitted solution resistance (R_s) and charge transfer resistance (R_{ct}) values of MoS₂, MoO₃@MoS₂, and MoO₃ after 1st cycle; Table S4: Fitted solution resistance (R_s) and charge transfer resistance (R_{ct}) values of MoS₂, MoO₃@MoS₂, and MoO₃ after 30th cycle; Table S5: Comparative table depicting electrochemical performance of selected TMO/TMS and/or carbon hybrids. References [33,36,54–58] were cited in Supplementary Materials.

Author Contributions: M.F.: conceptualization; investigation; visualization; writing—original draft. S.H.: investigation. M.I.: investigation; supervision; writing—review and editing. J.-Y.K., D.H., J.-H.B., D.V., B.A., S.A., H.-S.K., A.N.S. and J.J.: investigation. K.-W.N.: conceptualization; funding acquisition; resources; supervision; writing—review and editing. All authors have read and agreed to the published version of the manuscript.

Funding: This work was supported by the Ministry of Trade, Industry & Energy (MOTIE, grant No. 20012318) and by the Ministry of SMEs and Startups (MSS, grant No. S3126915).

Data Availability Statement: The data presented in this study are available on request from the corresponding author.

Conflicts of Interest: The authors declare no conflict of interest.

References

1. Luo, W.; Shen, F.; Bommier, C.; Zhu, H.; Ji, X.; Hu, L. Na-Ion Battery Anodes: Materials and Electrochemistry. *Acc. Chem. Res.* **2016**, *49*, 231–240. [[CrossRef](#)] [[PubMed](#)]
2. Chu, S.; Majumdar, A. Opportunities and challenges for a sustainable energy future. *Nature* **2012**, *488*, 294–303. [[CrossRef](#)] [[PubMed](#)]
3. Ding, Y.; Cano, Z.P.; Yu, A.; Lu, J.; Chen, Z. Automotive Li-Ion Batteries: Current Status and Future Perspectives. *Electrochem. Energy Rev.* **2019**, *2*, 1–28. [[CrossRef](#)]
4. Liang, Y.; Zhao, C.Z.; Yuan, H.; Chen, Y.; Zhang, W.; Huang, J.Q.; Yu, D.; Liu, Y.; Titirici, M.M.; Chueh, Y.L.; et al. A review of rechargeable batteries for portable electronic devices. *InfoMat* **2019**, *1*, 6–32. [[CrossRef](#)]
5. Buqa, H.; Goers, D.; Holzappel, M.; Spahr, M.E.; Novák, P. High Rate Capability of Graphite Negative Electrodes for Lithium-Ion Batteries. *J. Electrochem. Soc.* **2005**, *152*, A474. [[CrossRef](#)]
6. Wang, X.; Zhang, Z.; Chen, Y.; Qu, Y.; Lai, Y.; Li, J. Morphology-controlled synthesis of MoS₂ nanostructures with different lithium storage properties. *J. Alloys Compd.* **2014**, *600*, 84–90. [[CrossRef](#)]
7. Zhang, S.; Chowdari, B.V.R.; Wen, Z.; Jin, J.; Yang, J. Constructing Highly Oriented Configuration by Few-Layer MoS₂: Toward High-Performance Lithium-Ion Batteries and Hydrogen Evolution Reactions. *ACS Nano* **2015**, *9*, 12464–12472. [[CrossRef](#)]
8. Radovsky, G.; Popovitz-Biro, R.; Staiger, M.; Gartsman, K.; Thomsen, C.; Lorenz, T.; Seifert, G. Tenne, Synthesis of copious amounts of SnS₂ and SnS₂/SnS nanotubes with ordered superstructures. *Angew. Chem.* **2011**, *123*, 12524–12528. [[CrossRef](#)]
9. Vikraman, D.; Hussain, S.; Prasanna, K.; Karuppasamy, K.; Jung, J.; Kim, H.-S. Facile method to synthesis hybrid phase 1T@2H MoSe₂ nanostructures for rechargeable lithium ion batteries. *J. Electroanal. Chem.* **2019**, *833*, 333–339. [[CrossRef](#)]
10. Hussain, S.; Faizan, M.; Vikraman, D.; Rabani, I.; Ali, B.; Kim, H.-S.; Jung, J.; Nam, K.-W. Eutectoid WxC embedded WS₂ nanosheets as a hybrid composite anode for lithium-ion batteries. *Ceram. Int.* **2021**, *47*, 18646–18655. [[CrossRef](#)]
11. Islam, M.; Jeong, M.-G.; Ali, G.; Oh, I.-H.; Chung, K.Y.; Sun, Y.-K.; Jung, H.-G. A 4 V Li-ion battery using all-spinel-based electrodes. *ChemSusChem* **2018**, *11*, 2165–2170. [[CrossRef](#)] [[PubMed](#)]
12. Islam, M.; Ali, G.; Akbar, M.; Ali, B.; Jeong, M.; Kim, J.; Chung, K.Y.; Nam, K.; Jung, H. Investigating the energy storage performance of the ZnMn₂O₄ anode for its potential application in lithium-ion batteries. *Int. J. Energy Res.* **2022**, *46*, 6444–6456. [[CrossRef](#)]
13. Feng, Y.; Liu, H.; Liu, Y.; Li, J. Tunable oxygen deficient in MoO_{3-x}/MoO₂ heterostructure for enhanced lithium storage properties. *Int. J. Energy Res.* **2022**, *46*, 5789–5799. [[CrossRef](#)]
14. Madian, M.; Eychmüller, A.; Giebeler, L. Current Advances in TiO₂-Based Nanostructure Electrodes for High Performance Lithium Ion Batteries. *Batteries* **2018**, *4*, 7. [[CrossRef](#)]
15. Chen, Z.; Belharouak, I.; Sun, Y.-K.; Amine, K. Titanium-Based Anode Materials for Safe Lithium-Ion Batteries. *Adv. Funct. Mater.* **2013**, *13*, 959–969. [[CrossRef](#)]
16. Ding, R.; Huang, Y.; Li, G.; Liao, Q.; Wei, T.; Liu, Y.; Huang, Y.; He, H. Carbon Anode Materials for Rechargeable Alkali Metal Ion Batteries and in-situ Characterization Techniques. *Front. Chem.* **2020**, *8*, 607504. [[CrossRef](#)]
17. Xiong, D.; Li, X.; Bai, Z.; Shan, H.; Fan, L.; Wu, C.; Li, D.; Lu, S. Superior Cathode Performance of Nitrogen-Doped Graphene Frameworks for Lithium Ion Batteries. *ACS Appl. Mater. Interfaces* **2017**, *9*, 10643–10651. [[CrossRef](#)]
18. Chen, Y.M.; Yu, X.Y.; Li, Z.; Paik, U.; Lou, X.W. Hierarchical MoS₂ tubular structures internally wired by carbon nanotubes as a highly stable anode material for lithium-ion batteries. *Sci. Adv.* **2016**, *2*, e1600021. [[CrossRef](#)]
19. Liu, X.; Wang, Y.; Yang, Y.; Lv, W.; Lian, G.; Golberg, D.; Wang, X.; Zhao, X.; Ding, Y. A MoS₂/carbon hybrid anode for high-performance li-ion batteries at low temperature. *Nano Energy* **2020**, *70*, 104550. [[CrossRef](#)]
20. Nzereogu, P.; Omah, A.; Ezema, F.; Iwuoha, E.; Nwanya, A. Anode materials for lithium-ion batteries: A review. *Appl. Surf. Sci. Adv.* **2022**, *9*, 100233. [[CrossRef](#)]
21. Yan, Y.; Liu, Y.; Zhang, Y.; Qin, C.; Yu, H.; Bakenov, Z.; Wang, Z. Sn modified nanoporous Ge for improved lithium storage performance. *J. Colloid Interface Sci.* **2021**, *602*, 563–572. [[CrossRef](#)] [[PubMed](#)]
22. Li, H.; Yamaguchi, T.; Matsumoto, S.; Hoshikawa, H.; Kumagai, T.; Okamoto, N.L.; Ichitsubo, T. Circumventing huge volume strain in alloy anodes of lithium batteries. *Nat. Commun.* **2020**, *11*, 1584. [[CrossRef](#)] [[PubMed](#)]

23. Fang, S.; Bresser, D.; Passerini, S. Transition Metal Oxide Anodes for Electrochemical Energy Storage in Lithium- and Sodium-Ion Batteries. *Adv. Energy Mater.* **2020**, *10*, 1902485. [[CrossRef](#)]
24. Reddy, M.V.; Rao, G.V.S.; Chowdari, B.V.R. Metal Oxides and Oxysalts as Anode Materials for Li Ion Batteries. *Chem. Rev.* **2013**, *113*, 5364–5457. [[CrossRef](#)] [[PubMed](#)]
25. Zhao, J.; Zhang, Y.; Wang, Y.; Li, H.; Peng, Y. The application of nanostructured transition metal sulfides as anodes for lithium ion batteries. *J. Energy Chem.* **2018**, *27*, 1536–1554. [[CrossRef](#)]
26. Xu, X.; Liu, W.; Kim, Y.; Cho, J. Nanostructured transition metal sulfides for lithium ion batteries: Progress and challenges. *Nano Today* **2014**, *9*, 604–630. [[CrossRef](#)]
27. Zhang, G.; Liu, H.; Qu, J.; Li, J. Two-dimensional layered MoS₂: Rational design, properties and electrochemical applications. *Energy Environ. Sci.* **2016**, *9*, 1190–1209. [[CrossRef](#)]
28. Wu, J.; Ihsan-Ul-Haq, M.; Ciucci, F.; Huang, B.; Kim, J.-K. Rationally designed nanostructured metal chalcogenides for advanced sodium-ion batteries. *Energy Storage Mater.* **2021**, *34*, 582–628. [[CrossRef](#)]
29. Kumar, V.P.; Panda, D.K. Review-next generation 2D material molybdenum disulfide (MoS₂): Properties, applications and challenges. *ECS J. Solid State Sci. Technol.* **2022**, *11*, 033012. [[CrossRef](#)]
30. Zuo, J.-H.; Zhai, P.-B.; He, Q.-Q.; Wang, L.; Chen, Q.; Gu, X.-K.; Yang, Z.-L.; Gong, Y.-J. In-situ constructed three-dimensional MoS₂-MoN heterostructure as the cathode of lithium-sulfur battery. *Rare Met.* **2022**, *41*, 1743–1752. [[CrossRef](#)]
31. Zhang, L.; Sun, D.; Kang, J.; Feng, J.; Bechtel, H.A.; Wang, L.-W.; Cairns, E.J.; Guo, J. Electrochemical Reaction Mechanism of the MoS₂ Electrode in a Lithium-Ion Cell Revealed by in Situ and Operando X-ray Absorption Spectroscopy. *Nano Lett.* **2018**, *18*, 1466–1475. [[CrossRef](#)] [[PubMed](#)]
32. Liao, J.-Y.; de Luna, B.; Manthiram, A. TiO₂-B nanowire arrays coated with layered MoS₂ nanosheets for lithium and sodium storage. *J. Mater. Chem. A* **2016**, *4*, 801–806. [[CrossRef](#)]
33. Chang, K.; Chen, W.-X.; Li, H.; Li, H. Microwave-assisted synthesis of SnS₂/SnO₂ composites by l-cysteine and their electrochemical performances when used as anode materials of Li-ion batteries. *Electrochim. Acta* **2011**, *56*, 2856–2861. [[CrossRef](#)]
34. Deng, Z.; Hu, Y.; Ren, D.; Lin, S.; Jiang, H.; Li, C. Reciprocal hybridization of MoO₂ nanoparticles and few-layer MoS₂ for stable lithium-ion batteries. *Chem. Commun.* **2015**, *51*, 13838–13841. [[CrossRef](#)]
35. Villevieille, C.; Wang, X.-J.; Krumeich, F.; Nesper, R.; Novák, P. MoS₂ coating on MoO₃ nanobelts: A novel approach for a high specific charge electrode for rechargeable Li-ion batteries. *J. Power Sources* **2015**, *279*, 636–644. [[CrossRef](#)]
36. Hu, C.; Shu, H.; Shen, Z.; Zhao, T.; Liang, P.; Chen, X. Hierarchical MoO₃/SnS₂ core-shell nanowires with enhanced electrochemical performance for lithium-ion batteries. *Phys. Chem. Chem. Phys.* **2018**, *20*, 17171–17179. [[CrossRef](#)]
37. Qu, B.; Sun, Y.; Liu, L.; Li, C.; Yu, C.; Zhang, X.; Chen, Y. Ultrasmall Fe₂O₃ nanoparticles/MoS₂ nanosheets composite as high-performance anode material for lithium ion batteries. *Sci. Rep.* **2017**, *7*, 42772. [[CrossRef](#)]
38. Li, Z.; Sun, P.; Zhan, X.; Zheng, Q.; Feng, T.; Braun, P.V.; Qi, S. Metallic 1T phase MoS₂/MnO composites with improved cyclability for lithium-ion battery anodes. *J. Alloys Compd.* **2019**, *796*, 25–32. [[CrossRef](#)]
39. Ahmed, B.; Anjum, D.H.; Hedhili, M.N.; Alshareef, H.N. Mechanistic insight into the stability of HfO₂-coated MoS₂ nanosheet anodes for sodium ion batteries. *Small* **2015**, *11*, 4341–4350. [[CrossRef](#)]
40. Ryu, W.-H.; Wilson, H.; Sohn, S.; Li, J.; Tong, X.; Shaulsky, E.; Schroers, J.; Elimelech, M.; Taylor, A.D. Heterogeneous WS_x/WO₃ thorn-bush nanofiber electrodes for sodium-ion batteries. *ACS Nano* **2016**, *10*, 3257–3266. [[CrossRef](#)]
41. Xie, J.; Zhang, J.; Li, S.; Grote, F.; Zhang, X.; Zhang, H.; Wang, R.; Lei, Y.; Pan, B.; Xie, Y. Controllable Disordered Engineering in Oxygen-Incorporated MoS₂ Ultrathin Nanosheets for Efficient Hydrogen Evolution. *J. Am. Chem. Soc.* **2013**, *135*, 17881–17888. [[CrossRef](#)] [[PubMed](#)]
42. Mishra, N.; Rathore, D.; Pandey, R.K. A comparative study of conventional type II and inverted core-shell nanostructures based on CdSe and ZnS. *Opt. Quantum Electron.* **2018**, *50*, 107. [[CrossRef](#)]
43. Li, H.; Zhang, Q.; Yap, C.C.R.; Tay, B.K.; Edwin, T.H.T.; Olivier, A.; Baillargeat, D. From Bulk to Monolayer MoS₂: Evolution of Raman Scattering. *Adv. Funct. Mater.* **2012**, *22*, 1385–1390. [[CrossRef](#)]
44. Sinaim, H.; Ham, D.J.; Lee, J.S.; Phuruangrat, A.; Thongtem, S.; Thongtem, T. Free-polymer controlling morphology of α-MoO₃ nanobelts by a facile hydrothermal synthesis, their electrochemistry for hydrogen evolution reactions and optical properties. *J. Alloys Compd.* **2012**, *516*, 172–178. [[CrossRef](#)]
45. Vikraman, D.; Liu, H.; Hussain, S.; Karuppasamy, K.; Youi, H.-K.; Jung, J.; Kang, J.; Kim, H.-S. Influence of morphological tuned nanostructure hybrid layers on efficient bulk heterojunction organic solar cell and X-ray detector performances. *Appl. Surf. Sci.* **2021**, *543*, 148863. [[CrossRef](#)]
46. Kim, S.S.; Britcher, L.; Kumar, S.; Griesser, H.J. XPS Study of Sulfur and Phosphorus Compounds with Different Oxidation States. *Sains Malays.* **2018**, *47*, 1913–1922. [[CrossRef](#)]
47. Dahl-Petersen, C.; Šarić, M.; Brorson, M.; Moses, P.G.; Rossmesl, J.; Lauritsen, J.V.; Helveg, S. Topotactic Growth of Edge-Terminated MoS₂ from MoO₂ Nanocrystals. *ACS Nano* **2018**, *12*, 5351–5358. [[CrossRef](#)]
48. Hussain, S.; Rabani, I.; Vikraman, D.; Feroze, A.; Ali, M.; Seo, Y.-S.; Song, W.; An, K.-S.; Kim, H.-S.; Chun, S.-H.; et al. MoS₂@X₂C (X = Mo or W) hybrids for enhanced supercapacitor and hydrogen evolution performances. *Chem. Eng. J.* **2020**, *421*, 127843. [[CrossRef](#)]
49. Brezesinski, T.; Wang, J.; Tolbert, S.H.; Dunn, B. Ordered mesoporous α-MoO₃ with iso-oriented nanocrystalline walls for thin-film pseudocapacitors. *Nat. Mater.* **2010**, *9*, 146–151. [[CrossRef](#)]

50. Zhou, K.; Zhou, W.; Liu, X.; Sang, Y.; Ji, S.; Li, W.; Lu, J.; Li, L.; Niu, W.; Liu, H. Ultrathin MoO₃ nanocrystal self-assembled on graphene nanosheets via oxygen bonding as supercapacitor electrodes of high capacitance and long cycle life. *Nano Energy* **2015**, *12*, 510–520. [[CrossRef](#)]
51. Zhang, H.; Lin, H.; Zheng, Y.; Hu, Y.; MacLennan, A. Understanding of the effect of synthesis temperature on the crystallization and activity of nano-MoS₂ catalyst. *Appl. Catal. B Environ.* **2015**, *165*, 537–546. [[CrossRef](#)]
52. Wang, Q.; Li, J. Facilitated lithium storage in MoS₂ overlayers supported on coaxial carbon nanotubes. *J. Phys. Chem. C* **2007**, *111*, 1675–1682. [[CrossRef](#)]
53. Cao, D.; Dai, Y.; Xie, S.; Wang, H.; Niu, C. Pyrolytic synthesis of MoO₃ nanoplates within foam-like carbon nanoflakes for enhanced lithium ion storage. *J. Colloid Interface Sci.* **2018**, *514*, 686–693. [[CrossRef](#)] [[PubMed](#)]
54. Li, X.; Li, W.; Li, M.; Cui, P.; Chen, D.; Gengenbach, T.; Chu, L.; Liu, H.; Song, G. Glucose-assisted synthesis of the hierarchical TiO₂ nanowire@MoS₂ nanosheet nanocomposite and its synergistic lithium storage performance. *J. Mater. Chem. A* **2015**, *3*, 2762–2769. [[CrossRef](#)]
55. Li, X.; Fu, J.; Sun, Y.; Sun, M.; Cheng, S.; Chen, K.; Yang, X.; Lou, Q.; Xu, T.; Shang, Y.; et al. Design and understanding of core/branch-structured VS₂ nanosheets@CNTs as high-performance anode materials for lithium-ion batteries. *Nanoscale* **2019**, *11*, 13343–13353. [[CrossRef](#)]
56. Zhu, K.; Wang, X.; Liu, J.; Li, S.; Wang, H.; Yang, L.; Liu, S.; Xie, T. Novel amorphous MoS₂/MoO₃/nitrogen-doped carbon composite with excellent electrochemical performance for lithium ion batteries and sodium ion batteries. *ACS Sustain. Chem. Eng.* **2017**, *5*, 8025–8034. [[CrossRef](#)]
57. Yang, X.; Zhang, Z.; Fu, Y.; Li, Q. Porous hollow carbon spheres decorated with molybdenum diselenide nanosheets as anodes for highly reversible lithium and sodium storage. *Nanoscale* **2015**, *7*, 10198–10203. [[CrossRef](#)]
58. Liu, M.; Gao, H.; Hu, G.; Zhu, K.; Huang, H. Facile preparation of core-shell Si@Li₄Ti₅O₁₂ nanocomposite as large-capacity lithium-ion battery anode. *J. Energy Chem.* **2020**, *40*, 89–98. [[CrossRef](#)]